


Oxygen Reduction Reaction *Hot Paper*

How to cite:

International Edition: doi.org/10.1002/anie.202209746

German Edition: doi.org/10.1002/ange.202209746

Atomically Dispersed Pentacoordinated-Zirconium Catalyst with Axial Oxygen Ligand for Oxygen Reduction Reaction

Xia Wang⁺, Yun An⁺, Lifeng Liu, Lingzhe Fang, Yannan Liu, Jiaxu Zhang, Haoyuan Qi, Thomas Heine, Tao Li, Agnieszka Kuc,* Minghao Yu,* and Xinliang Feng*

Abstract: Single-atom catalysts (SACs), as promising alternatives to Pt-based catalysts, suffer from the limited choice of center metals and low single-atom loading. Here, we report a pentacoordinated Zr-based SAC with nontrivial axial O ligands (denoted O–Zr–N–C) for oxygen reduction reaction (ORR). The O ligand downshifts the d-band center of Zr and confers Zr sites with stable local structure and proper adsorption capability for intermediates. Consequently, the ORR performance of O–Zr–N–C prominently surpasses that of commercial Pt/C, achieving a half-wave potential of 0.91 V vs. reversible hydrogen electrode and outstanding durability (92 % current retention after 130-hour operation). Moreover, the Zr site shows good resistance towards aggregation, enabling the synthesis of Zr-based SAC with high loading (9.1 wt%). With the high-loading catalyst, the zinc-air battery (ZAB) delivers a record-high power density of 324 mWcm⁻² among those of SAC-based ZABs.

Introduction

The electrochemical oxygen reduction reaction (ORR), converting O₂ to OH⁻ in alkaline medium, via a four-electron route, is one of the most important heterogeneous reactions for sustainable energy conversion technologies like metal–air batteries and fuel cells.^[1] By minimizing the overpotential of ORR, electrocatalysts hold the central role in determining the overall output power efficiency of these energy conversion devices.^[2] Today, platinum-based catalysts represent the benchmark ORR catalysts in commercialization, which, however, suffer from low crustal abundance, high cost, and inferior durability.^[3] In this regard, developing novel non-precious ORR catalysts as alternatives to platinum-based catalysts has been a focal research direction over the past decades.

Transition-metal single-atom catalysts (SACs) have sparked widespread interest in the field of electrocatalysis owing to their fascinating virtues, such as maximized atom utilization, flexible coordination structure regulation, and superb catalytic selectivity and activity.^[4] These SACs are normally composed of single transition metal atom immobilized in N-doped carbon matrix by in-plane coordinating C or N atoms.^[5] To promote catalytic activity, intensive efforts

[*] Dr. X. Wang,⁺ Dr. Y. Liu, J. Zhang, Dr. M. Yu, Prof. X. Feng
 Center for Advancing Electronics Dresden (cfaed) & Faculty of
 Chemistry and Food Chemistry, Technische Universität Dresden
 01062 Dresden (Germany)
 E-mail: minghao.yu@tu-dresden.de
 xinliang.feng@tu-dresden.de

Dr. X. Wang⁺
 Max-Planck-Institute for Chemical Physics of Solids
 01187 Dresden (Germany)

Dr. Y. An,⁺ Prof. T. Heine
 Theoretical Chemistry, Technische Universität Dresden
 01062 Dresden (Germany)

Dr. Y. An,⁺ Prof. T. Heine, Dr. A. Kuc
 Helmholtz-Zentrum Dresden-Rossendorf, Abteilung Ressourcenö-
 kologie, Forschungsstelle Leipzig
 04318 Leipzig (Germany)
 E-mail: a.kuc@hzdr.de

Dr. L. Liu
 Clean Energy Cluster
 International Iberian Nanotechnology Laboratory (INL)
 4715-330 Braga (Portugal)

L. Fang, Prof. T. Li
 Department of Chemistry and Biochemistry
 Northern Illinois University
 DeKalb, IL 60115 (USA)

Dr. H. Qi
 Central Facility of Materials Science Electron Microscopy, University
 of Ulm
 89081 Ulm (Germany)

Prof. T. Heine
 Department of Chemistry, Yonsei University
 Seoul 03722 (Korea)

Prof. T. Li
 X-ray Science Division, Argonne National Laboratory
 Lemont, IL 60439 (USA)

Prof. X. Feng
 Max Planck Institute of Microstructure Physics
 06120 Halle (Germany)

[⁺] These authors contributed equally to this work.

© 2022 The Authors. Angewandte Chemie International Edition published by Wiley-VCH GmbH. This is an open access article under the terms of the Creative Commons Attribution Non-Commercial NoDerivs License, which permits use and distribution in any medium, provided the original work is properly cited, the use is non-commercial and no modifications or adaptations are made.

have been devoted to exploring the principle of how metal atom centers and in-plane coordinating atoms manipulate the binding energy of SACs with reaction intermediates. The accumulated understanding has further brought out diverse strategies for regulating the active sites of SACs, such as in-plane coordination number control (e.g., 1–4),^[6] in-plane heteroatom doping (e.g., B, P or S),^[4b,6b,7] and hetero-metal centers design (e.g., Fe–Pt, Fe–Ni, Cu–Zn).^[8] However, non-precious SACs with platinum-competitive ORR activity developed to date are still limited to only a few metal elements (e.g., Fe, Co, Mn, and Zn),^[9] which is most likely due to the relative simplicity of the in-plane-coordination configuration. On the other hand, metal atoms in SACs typically show high surface free energy and tend to aggregate into metal clusters or nanoparticles under the conventional synthesis conditions of SACs (i.e., high-temperature pyrolysis). As a result, the obtained SACs generally suffer from low metal loading (<5 wt%),^[10] and thus their limited performance would be reflected by the usage in energy conversion devices under high operating current densities.^[11] For example, the maximum output power of zinc-air batteries (ZABs) based on SAC cathodes remains below 200 mW cm⁻².

In this study, we discover a Zr-based SAC with single-atom Zr sites featured by a pentacoordination configuration with nontrivial axial O ligands (denoted O–Zr–N–C). The quantum-mechanical simulations indicate the significant role of axial O ligand in lowering the d-band center of Zr and weakening the adsorption energy of O-intermediates on single-atom Zr sites, which empowers O–Zr–N–C with platinum-competitive ORR activity. In 0.1 M KOH electrolyte, the O–Zr–N–C catalyst exhibits a high halfwave potential of 0.91 V vs. reversible hydrogen electrode (RHE), an impressive kinetic current density of 76.0 mA cm⁻² at 0.80 V vs. RHE, and ultralong durability with 92% current retention after 130-hour operation at 0.70 V vs. RHE, surpassing the state-of-the-art SACs. Besides, the unique pentacoordination configuration of the single-atom Zr sites is resistant to atom aggregation, which enables the synthesis of O–Zr–N–C catalyst with a high Zr loading (9.1 wt%). ZAB assembled with this high-loading catalyst achieves a superior power density of 324 mW cm⁻², which represents the state-of-the-art among those reported SAC-based ZABs.

Results and Discussion

Figure 1a schematically illustrates the synthetic route of O–Zr–N–C. Typically, 2-methylimidazole (MIM) and two types of silica spheres (diameters of 220 nm and 12 nm, Figure S1) were added into distilled water and sonicated into a homogeneous dispersion. A mixed solution of ZrCl₄ and ZnCl₂ dissolved in ethanol was subsequently dropwise added into the above water dispersion under stirring. During this process, ZrCl₄ hydrolysed to ZrOCl₂ in the mixture,^[12] and the obtained ZrOCl₂ served as the precursor of single atom Zr with an axial O ligand. Meanwhile, silica spheres and ZnCl₂ worked as pore-producing templates to empower

the synthesized catalyst with a hierarchical porous structure. The solvent of the mixture was then removed by rotary evaporation, and the collected solid composite (Zr-MIM@-SiO₂) was annealed at 950 °C for 2 hours in an Ar atmosphere. Finally, O–Zr–N–C was obtained by washing with diluted hydrofluoric acid solution.

We first explored the obtained catalyst with a Zr loading of 3.1 wt% (quantified by the inductively coupled plasma optical emission spectrometry (ICP-OES)). Without specification in this article, O–Zr–N–C refers to the catalyst with a Zr loading of 3.1 wt%. Scanning electron microscopy (SEM, Figure 1b) and high-angle annular dark-field scanning transmission electron microscopy (HAADF-STEM, Figure 1c) images of O–Zr–N–C uncover its hierarchical porous structure with abundant mesopores and macropores, whose diameters correspond well with the size of silica templates. By analysing the N₂ adsorption-desorption isotherm curves (Figure S2), O–Zr–N–C was demonstrated to have a large Brunauer–Emmett–Teller (BET) surface area of 1343 m² g⁻¹. Moreover, the pore size distribution analysis of O–Zr–N–C shows the presence of both micropores (≈1.0 nm) and mesopores (≈11 nm). It is well established that micropores are able to increase the density of exposed active sites, mesopores are beneficial to the mass transfer, and macropores contribute to the reaction kinetics, thus synergistically improving the catalytic activity.^[13]

High-resolution HAADF-STEM image (Figure 1d) further displays plentiful bright spots distributed in the carbon matrix. No metal-related nanoparticles were identified in the images, which is also supported by the X-ray diffraction pattern of O–Zr–N–C (Figure S3a). Moreover, the elemental distribution of O–Zr–N–C was assessed by the electron energy loss spectroscopy (EELS)-elemental mapping analysis. The acquired elemental mapping images (Figure 1e) corroborate the uniform distribution of C, N, O, and Zr at the nanometer scale, without the presence of other impurities like Zn and Cl. The Zr loading in O–Zr–N–C was estimated to be 3.5 wt% by the elemental mapping analysis, which agrees well with the ICP-OES result. Besides, the co-existence of C, N, O, and Zr within an Ångström-scale region implies that Zr atoms are fixed in the carbon matrix by coordinating with C, N, and O atoms. (Figure 1f–i, Note S1).

The chemical composition of O–Zr–N–C was further characterized by X-ray photoelectron spectroscopy (XPS, Figure S4). Only C, N, O, and Zr were detected, and other impurities like Zn and Cl were not present (Table S1). In the N 1s spectrum (Figure 2a), apart from pyridinic N (398.1 eV), pyrrolic N (399.6 eV), graphitic N (400.9 eV), and oxidized N (403.3 eV), an additional peak located at 398.7 eV was observed, corresponding to N atoms coordinated with Zr (Zr–N_x).^[2c,14] Additionally, as shown in Figure S5, O–Zr–N–C displays a Zr 3d_{5/2} peak (182.4 eV) located between Zr^{III} (182.3 eV) and Zr^{IV} (182.7 eV).^[15] This result indicates that the average valence state of Zr species in O–Zr–N–C is situated between Zr²⁺ and Zr⁴⁺.

Next, Zr K-edge X-ray absorption spectra were collected to gain a closer insight into the local coordination structure of Zr in O–Zr–N–C. In the X-ray absorption near edge

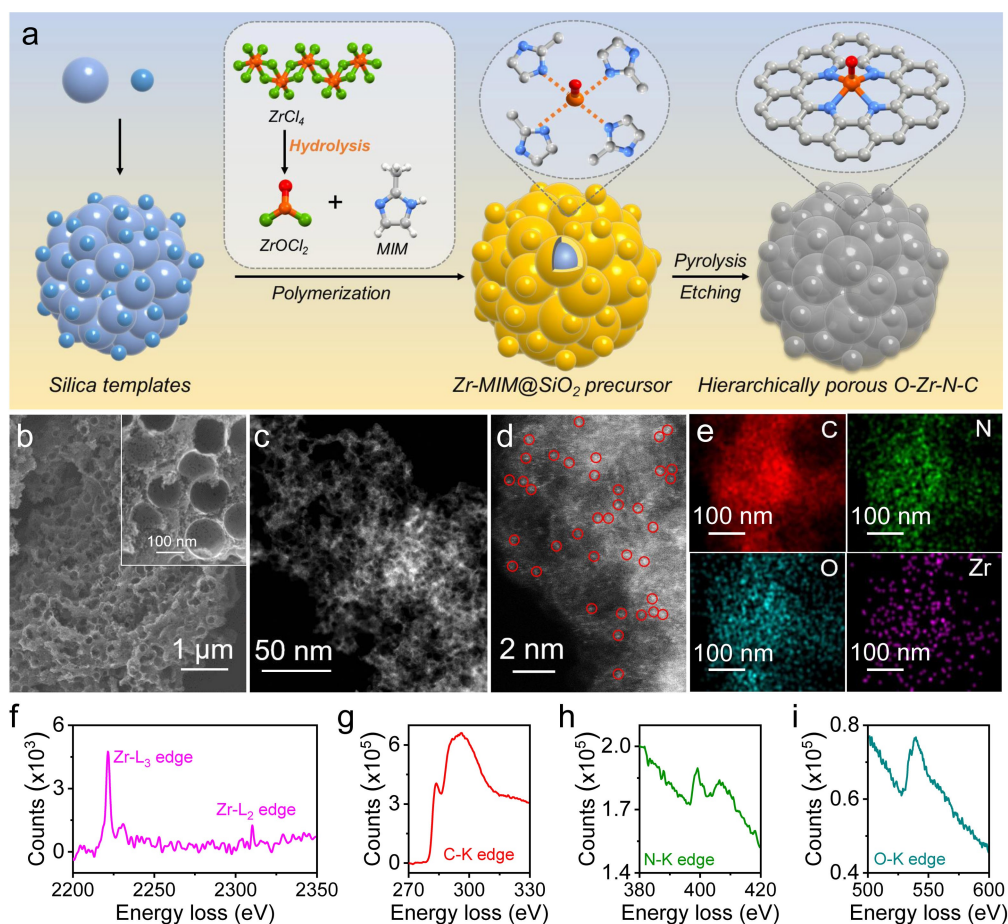


Figure 1. Synthesis and characterization of O–Zr–N–C catalyst. a) Schematic illustrating the synthetic route of O–Zr–N–C. b) SEM, c) HAADF-STEM, and d) high-resolution HAADF-STEM images of O–Zr–N–C. The distinct bright dots (circled in red) in (d) indicate that Zr is atomically dispersed in the N-doped carbon matrix. e) EELS elemental mappings of O–Zr–N–C. f–i) EELS spectra derived from the zone near one bright dot in (d), implying the local chemical environment of f) Zr with g) C, h) N, and i) O.

structure (XANES) spectra (Figure 2b), the absorption threshold energy of O–Zr–N–C is located between those of ZrN and ZrO₂. The first-derivative XANES curves of three reference samples (i.e., ZrO₂, ZrN, and Zr foil) were derived, and the linear relationship between the photon energy at the maximum intensity (E_0) and the valence state was well established (inset in Figure 2b). Accordingly, the average valence of Zr in O–Zr–N–C can be quantified to be 3.3+, which is in good agreement with the Zr valence estimated from the XPS result. Figure 2c shows the Zr K-edge Fourier transform k^3 -weighted extended X-ray absorption fine structure (EXAFS) spectra of O–Zr–N–C and other reference samples. O–Zr–N–C displays the dominant contribution of the first-shell peak at 1.42 Å, corresponding to Zr coordinated by light atoms (e.g., N, C, and O). Moreover, the atomically dispersed feature of Zr in O–Zr–N–C is evidenced by the absence of Zr–Zr and Zr–O–Zr peaks (i.e., the peak at 2.8 Å in Zr foil and the peak at 2.9 Å in ZrO₂).

Importantly, the Zr EXAFS spectrum of O–Zr–N–C was fitted assuming a variable number of in-plane coordinated N or C atoms and axial O atoms (Figure S6). The

best-fitting result elucidates the first-shell coordination structure of Zr in O–Zr–N–C (Figure 2d and Figure S7), in which Zr is coordinated by close to four (coordination number: 3.82) in-plane N or C atoms (bond length: 2.05 Å) and about one (coordination number: 1.40) axial O atom (bond length: 2.20 Å) (Table S2). Of note, the mismatch between the fitting result and experimental data along with the increase of radial distance (>2.5 Å) and k is assigned to the scattering of the out-shell atoms and inevitable disordered structure. Furthermore, wavelet transform was performed to demonstrate the Zr K-edge EXAFS oscillations owing to its powerful resolutions in both k and R spaces (Figure 2e–h).^[16] As expected, O–Zr–N–C depicts only one intensity maximum at around 4 Å⁻¹ (k -space), which contrasts with the intensity maximum of the three reference samples at around 9 Å⁻¹ (k -space). The above results confirm that Zr species in O–Zr–N–C exist in an isolated manner without the presence of Zr-related nanoparticles or clusters.

The ORR-electrocatalytic activity of O–Zr–N–C was evaluated by the rotating disk electrode (RDE) in an O₂-saturated 0.1 M KOH solution (pH=13). The Zr-free N-doped carbon catalyst (denoted as N–C, Figure S8) and the

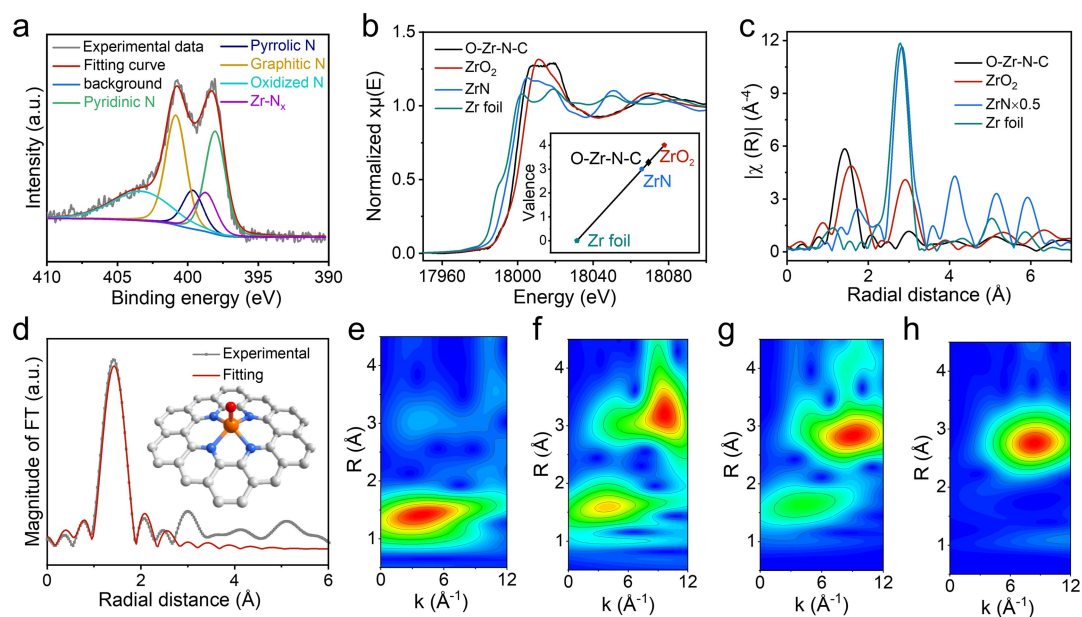


Figure 2. Configuration of single-atom Zr sites. a) N 1s XPS spectrum of O–Zr–N–C. Zr K-edge b) XANES and c) k^3 -weighted Fourier transform spectra of O–Zr–N–C, ZrO₂, ZrN, and Zr foil. d) The R space curve-fitting of O–Zr–N–C. Inset illustrates the fitted structure of the Zr site in O–Zr–N–C. The spheres in grey, blue, orange, and red represent C, N, Zr, and O atoms, respectively. The wavelet transforms for the k^3 -weighted Zr K-edge EXAFS of e) O–Zr–N–C, f) ZrO₂, g) ZrN, and h) Zr foil.

commercial Pt/C catalyst were also studied as references. Linear sweep voltammetry (LSV) curves of the three catalysts (Figure 3a) indicate the best activity of O–Zr–N–C with aspect to its highest halfwave potential ($E_{1/2}$). Specifically, $E_{1/2}$ of O–Zr–N–C, N–C, and Pt/C is 0.91 V, 0.82 V, and 0.86 V vs. RHE, respectively. Moreover, O–Zr–N–C exhibits a remarkable kinetic current density (J_k) of 76.0 mA cm⁻² at 0.80 V vs. RHE, about 10 times and 4.8 times higher than that of N–C (7.8 mA cm⁻²) and Pt/C (15.8 mA cm⁻²), respectively (Figure 3b). The lowest Tafel slope of O–Zr–N–C (66.1 mV dec⁻¹) among those of N–C (79.9 mV dec⁻¹) and Pt/C (89.7 mV dec⁻¹) also supports the superior ORR kinetics of O–Zr–N–C (Figure 3c).

We further investigated the ORR selectivity of O–Zr–N–C using the rotating ring-disk electrode measurement (Figure 3d). The H₂O₂ yield collected from O–Zr–N–C is below $\approx 8.0\%$ at potentials from 0 to 0.90 V vs. RHE, corresponding to the electron transfer number of 3.87–4.00. The result demonstrates that O–Zr–N–C undergoes a more efficient four-electron pathway than the benchmark Pt/C (H₂O₂ yield: below $\approx 10.4\%$, electron transfer number: 3.79–3.94). Besides, the O–Zr–N–C catalyst exhibits ultralong ORR durability. In the chronoamperometry measurement at 0.70 V vs. RHE with an RDE rotating speed of 1600 rpm, O–Zr–N–C retains 92% of its initial current density after 130-hour operation, whereas the commercial Pt/C catalyst depicts a huge current loss of 43% only after 30 hours (Figure 3e). The catalytic stability of O–Zr–N–C and Pt/C was evaluated by the standard accelerated durability test between 0.60 and 1.00 V at a sweep rate of 100 mV s⁻¹. Significantly, $E_{1/2}$ of O–Zr–N–C showed a negligible decay of less than 1 mV and 2 mV after 10,000

and 40,000 continuous cycles, respectively, in sharp contrast with the large $E_{1/2}$ loss of Pt/C (20 mV after 2500 cycles and 41 mV after 10,000 cycles, the inset in Figure 3e). Moreover, high-resolution HAADF-STEM image of O–Zr–N–C after the stability test (Figure S9) indicates the well maintained single-atom Zr sites, further verifying the stable structural stability of O–Zr–N–C. Additionally, O–Zr–N–C demonstrates a good resistance towards methanol poisoning. In the chronoamperometry test, injecting 5% (v/v) methanol into the electrolyte caused drastically decreased current density of the Pt/C catalyst. By contrast, O–Zr–N–C displayed no obvious drop at the same test condition, reflecting its excellent methanol tolerance, demonstrating the strong anti-poisoning effect of O–Zr–N–C towards methanol. (Figure S10). Table S3 summarizes the overall ORR performance of recently reported transition metal-based SACs, justifying that O–Zr–N–C surpasses those state-of-the-art SACs (e.g., Fe-, Co-, Mn-, and Zn-based SACs) in terms of diverse parameters.

Density functional theory (DFT) calculations were performed to explore how the local coordination environment of Zr determines the catalytic mechanism. First, conventional in-plane quadra-coordinated Zr structures (i.e., Zr–N_{4-n}–C_n, $n=0, 2$ and 3) were investigated. As revealed, all Zr–N_{4-n}–C_n structures show extremely strong adsorption on O-containing intermediates (binding energy > 4 eV), which indicates the ultrahigh energy for the last step of OH* desorption from the catalysts, leading to poor ORR activity (Figure S11). Meanwhile, the strong adsorption energy of O-intermediates reflects high tendency of the in-plane quadra-coordinated Zr to link another axial O ligand. We thus calculated the formation energies of Zr–N_{4-n}–C_n and O

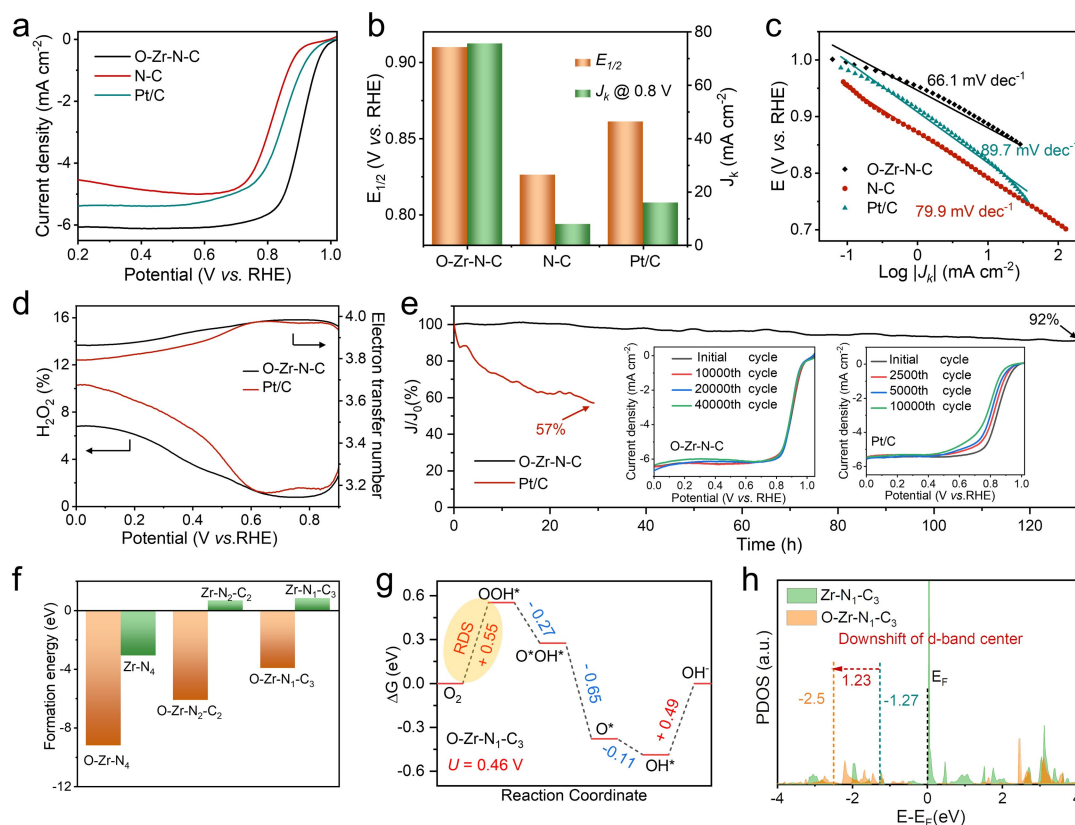


Figure 3. ORR performance and theoretical insights. a) ORR polarization curves at a scan rate of 5 mV s^{-1} with a rotating speed of 1600 rpm. b) $E_{1/2}$ and J_k of O-Zr-N-C, N-C, and Pt/C at 0.80 V vs. RHE. c) Tafel plots of O-Zr-N-C, N-C, and Pt/C. d) H_2O_2 yield and the calculated electron-transfer number of O-Zr-N-C and Pt/C. e) Chronoamperometric curves of O-Zr-N-C and Pt/C at 0.70 V vs. RHE. Inset of (e) displays the ORR polarization curves of O-Zr-N-C and Pt/C before and after accelerated durability tests. f) Formation energy of O-Zr-N_{4-n}-C_n and Zr-N_{4-n}-C_n ($n=0, 2$ and 3). g) ORR Gibbs free energy profiles on O-Zr-N₁-C₃ at the potential bias $U=0.46 \text{ V}$. h) PDOS of Zr sites in O-Zr-N₁-C₃ and Zr-N₁-C₃.

ligand-linked Zr-N_{4-n}-C_n (denoted O-Zr-N_{4-n}-C_n, $n=0, 2$ and 3). Of note, O-Zr-N₃-C₁ is not considered because of the unrealistic oxidation state of Zr. It is notable that the much lower formation energy (ΔE_f) of O-Zr-N_{4-n}-C_n (-9.22 eV of O-Zr-N₄, -6.12 eV of O-Zr-N₂-C₂, and -3.93 eV of O-Zr-N₁-C₃) than that of Zr-N_{4-n}-C_n (-3.08 eV of Zr-N₄, 0.68 eV of Zr-N₂-C₂, and 0.84 eV of Zr-N₁-C₃) manifests that the O-Zr-N_{4-n}-C_n structure is more energetically favourable than Zr-N_{4-n}-C_n motif (Figure 3f). The low formation energy of O-Zr-N_{4-n}-C_n also reflects the excellent chemical stability of the pentacoordinated Zr sites in the O-Zr-N-C catalyst, which inhibits the local structure collapse of Zr sites during the ORR process and explains the ultralong ORR durability of the O-Zr-N-C catalyst.

For an intuitive comparison, we further calculated the ORR Gibbs free energy profiles of O-Zr-N_{4-n}-C_n. Significantly decreased energy barriers are discovered for all O-Zr-N_{4-n}-C_n structures in comparison with the corresponding Zr-N_{4-n}-C_n structures (Figure S12 and S13), again demonstrating the high preference for O-Zr-N_{4-n}-C_n. Figure 3g illustrates the free energy profiles of O-Zr-N₁-C₃ (the optimal Zr configuration in terms of ORR overpotential). The OH* desorption energy of O-Zr-N₁-C₃

decreases to 0.49 eV compared with 5.32 eV in Zr-N₁-C₃. The ORR activity follows the order of O-Zr-N₁-C₃ > O-Zr-N₄ > O-Zr-N₂-C₂, with the overpotential of 0.55 V , 0.62 V , and 0.87 V , respectively.

Additional insights are gained by examining the d-band electronic structures of Zr centers, as the d-band center is recognized to well correlate with the metal-adsorbate interaction.^[17] Figure 3h compares the projected density of states (PDOS) of Zr in O-Zr-N₁-C₃ and Zr-N₁-C₃. The axial O ligand is verified to greatly lower the d-band center of Zr-N₁-C₃ from -1.27 eV to -2.50 eV , thus explaining the weakened adsorption energy of O-intermediates on O-Zr-N₁-C₃. Moreover, the downshift of d-band center is also found for other O-Zr-N_{4-n}-C_n structures in comparison with the corresponding Zr-N_{4-n}-C_n (Figure S14). Moreover, the Bader charge of Zr (0.41 e^-) in O-Zr-N₁-C₃ is lower than that of Zr (0.55 e^-) in Zr-N₁-C₃, which indicates the extra charge transfer between O and Zr in O-Zr-N₁-C₃ due to the electron-withdrawing axial O ligand. From this perspective, the lower charge in O-Zr-N₁-C₃ further indicates the weaker interaction between Zr and O-containing intermediates, enabling the easier desorption of OH*. These findings provide significant guidance for the future effort in modifying or re-designing Zr-based active sites via

diverse approaches (e.g., heteroatom coordination and hetero-metal sites).

The outstanding chemical stability of O–Zr–N–C inspires our hypothesis that the unique pentacoordinated Zr sites would show good resistance to metal aggregation, thus offering the opportunity to synthesize the O–Zr–N–C catalyst with high Zr loading (denoted as O–Zr–N–C–h). In this regard, we managed to obtain O–Zr–N–C–h via the routine pyrolysis approach by using excess ZrCl_4 precursor (8-fold amount). XRD spectrum, SEM and HAADF-STEM images, EELS mapping images, Zr K-edge XANES and k^3 -weighted Fourier transform of the EXAFS spectrum reflect that, compared with O–Zr–N–C, O–Zr–N–C–h shows a similar morphology and almost the same local coordination structure of Zr sites (Figure S15–S17). The Zr loading was measured to be 9.1 wt% by ICP-OES, predominantly larger than those of conventional SACs (typically <5 wt%, Table S3).

The ORR performance of O–Zr–N–C and O–Zr–N–C–h was further compared by the RDE test in the O_2 -saturated 0.1 M KOH solution. Indicated by the polarization curves (Figure 4a), O–Zr–N–C–h presents a slightly higher $E_{1/2}$ (0.92 V vs. RHE) and a bit smaller diffusion-limited current density (J_1 : 5.53 mA cm^{-2}) than O–Zr–N–C ($E_{1/2}$: 0.91 V vs. RHE, J_1 : 6.08 mA cm^{-2}). The decreased J_1 can be assigned to the decreased mass transport efficiency associated with the enhanced electron-transfer resistance (Figure S18) and the decreased micropore surface area of O–Zr–N–C–h (Figure S19 and Table S4). Compared with O–Zr–N–C (J_k : 76 mA cm^{-2} at 0.80 V vs. RHE), O–Zr–N–C–h achieves a significantly increased J_k of

104 mA cm^{-2} at 0.80 V vs. RHE. Furthermore, O–Zr–N–C–h shows a lower Tafel slope (58.3 mV dec^{-1}) than O–Zr–N–C (66.1 mV dec^{-1}), implying the superior ORR kinetics of O–Zr–N–C–h (Figure S20). With high Zr loading, O–Zr–N–C–h still maintains the ultralong ORR durability (Figure 4b). After 130-hour operation at 0.70 V vs. RHE, current retention of O–Zr–N–C–h reaches 93.6%, which is well comparable with that of O–Zr–N–C (92.0%).

Employing the high Zr-loading catalyst with superb J_k is supposed to enable the as-built energy conversion devices (operated at large current density) with outstanding output power capability. As a proof, we further assembled ZAB devices using O–Zr–N–C, O–Zr–N–C–h, and Pt/C as cathode catalysts, respectively. The open circuit voltage (OCV) of the O–Zr–N–C–h-based ZAB reached about 1.50 V (Figure S21), which is higher than those of the O–Zr–N–C-based ZAB (1.48 V) and Pt/C-based ZAB (1.45 V). The O–Zr–N–C-based ZAB delivered a maximum power density of 289 mW cm^{-2} , which is considerably higher than that of the Pt/C-based ZAB (121 mW cm^{-2}). More impressively, the maximum power density of O–Zr–N–C–h-based ZAB reached 324 mW cm^{-2} , which represents a record-high value among those of SACs-based ZABs (Figure 4c and Table S5). This result rationalizes the necessity of developing catalysts with dense active sites for energy conversion devices.

Finally, to highlight the operation durability of our catalysts, ZAB devices with continuously refilled Zn anodes were assessed by discharging at 10 mA cm^{-2} (Figure 4d). Fast voltage decay was discovered for the Pt/C-based ZAB, with the voltage dropping to 1.17 V after 100-hour oper-

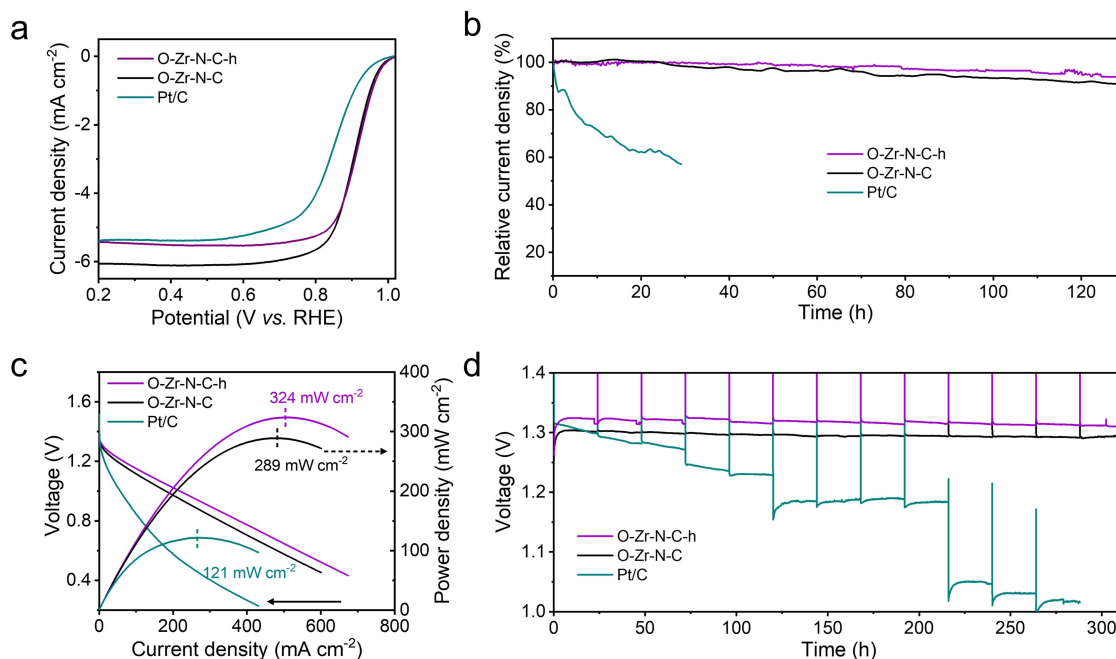


Figure 4. High Zr-loading catalyst for ZABs. a) ORR polarization curves of O–Zr–N–C–h, O–Zr–N–C, and Pt/C at a scan rate of 5 mV s^{-1} with a rotating speed of 1600 rpm. b) Chronoamperometric curves of O–Zr–N–C–h, O–Zr–N–C, and Pt/C at 0.70 V vs. RHE. c) Discharge polarization curves and corresponding power density curves of O–Zr–N–C–h, O–Zr–N–C, and Pt/C-based ZABs. d) Discharge curves of O–Zr–N–C–h, O–Zr–N–C, and Pt/C-based ZABs at 10 mA cm^{-2} with the continuously refilled Zn anode.

ation. By contrast, both O–Zr–N–C-based and O–Zr–N–C–h-based ZABs presented no noticeable voltage degradation after even 312 hours (13 cycles), verifying the feasibility of our catalysts for long-term use.

Conclusion

Overall, our work has demonstrated a new non-precious Zr-based SAC with platinum-competitive ORR activity in alkaline electrolyte. The unique pentacoordinated Zr site with a nontrivial axial O ligand empowers the obtained O–Zr–N–C catalyst with excellent ORR catalytic activity ($E_{1/2}$ of 0.91 V, kinetic current density of 76 mA cm^{-2} at 0.80 V vs. RHE), selectivity (<8% H_2O_2 yield), and durability (92% current retention after 130 hours). The superior chemical stability of single-atom Zr sites further allows the synthesis of high Zr-loading catalyst (9.1 wt%), which further enables the assembled SAC-based ZAB with a record-high power density (324 mW cm^{-2}). Moreover, theoretical modelling indicates the significant role of the axial O ligand in lowering the d-band center of Zr and weakening the adsorption energy of O-intermediates on Zr sites. These derived insights provide valuable guidance for modifying or re-designing better Zr-based SACs (e.g., as Fenton-inactive ORR catalysts in the acidic electrolyte). Additionally, our study highlights that, in addition to the in-plane coordination structure regulation, controlling the axial coordination could be a new design direction for advanced SACs towards ORR and other electrocatalytic processes.

Acknowledgements

This work was financially supported by European Union's Horizon 2020 research and innovation programme (GrapheneCore3 881603), Sächsisches Staatsministerium für Wissenschaft und Kunst (Sonderzuweisung zur Unterstützung profilbestimmender Struktureinheiten), German Research Foundation (DFG) within the Cluster of Excellence, and CRC 1415 (grant no. 417590517). X.W. gratefully acknowledges funding from China Scholarship Council. The authors acknowledge the use of the facilities in the Dresden Center for Nanoanalysis at the Technische Universität Dresden, the beamline B18 at Diamond Light Source (Didcot, England), and the Center for Information Services and High-Performance Computing (ZIH) at TU Dresden for generous allocations of compute resources. This research used resources of the Advanced Photon Source, a U.S. Department of Energy (DOE) Office of Science User Facility operated for the DOE Office of Science by Argonne National Laboratory under Contract No. AC02-06CH11357. The authors also thank Dongqi Li, Qiongqiong Lu, Peng Chen, Boya Sun, Junjie Wang, and Dr. Maximilian Springer for the insightful discussions. Open Access funding enabled and organized by Projekt DEAL.

Conflict of Interest

The authors declare no conflict of interest.

Data Availability Statement

The data that support the findings of this study are available from the corresponding author upon reasonable request.

Keywords: High Single-Atom Loading · Oxygen Reduction Reaction · Pentacoordinated Configuration · Single-Atom Catalysts · Zinc-Air Battery

- [1] a) M. Li, Z. Zhao, T. Cheng, A. Fortunelli, C.-Y. Chen, R. Yu, Q. Zhang, L. Gu, B. V. Merinov, Z. Lin, *Science* **2016**, *354*, 1414–1419; b) Y. Liang, Y. Li, H. Wang, J. Zhou, J. Wang, T. Regier, H. Dai, *Nat. Mater.* **2011**, *10*, 780–786; c) X. Wang, R. K. M. Raghupathy, C. J. Querebillo, Z. Liao, D. Li, K. Lin, M. Hantusch, Z. Sofer, B. Li, E. Zschech, *Adv. Mater.* **2021**, *33*, 2008752.
- [2] a) M. Shao, Q. Chang, J.-P. Dodelet, R. Chenitz, *Chem. Rev.* **2016**, *116*, 3594–3657; b) Z.-S. Wu, S. Yang, Y. Sun, K. Parvez, X. Feng, K. Müllen, *J. Am. Chem. Soc.* **2012**, *134*, 9082–9085; c) Y. Yuan, J. Wang, S. Adimi, H. Shen, T. Thomas, R. Ma, J. P. Attfield, M. Yang, *Nat. Mater.* **2020**, *19*, 282–286.
- [3] A. Chen, P. Holt-Hindle, *Chem. Rev.* **2010**, *110*, 3767–3804.
- [4] a) Y. Mun, S. Lee, K. Kim, S. Kim, S. Lee, J. W. Han, J. Lee, *J. Am. Chem. Soc.* **2019**, *141*, 6254–6262; b) J. Zhang, Y. Zhao, C. Chen, Y.-C. Huang, C.-L. Dong, C.-J. Chen, R.-S. Liu, C. Wang, K. Yan, Y. Li, *J. Am. Chem. Soc.* **2019**, *141*, 20118–20126; c) P. Li, M. Wang, X. Duan, L. Zheng, X. Cheng, Y. Zhang, Y. Kuang, Y. Li, Q. Ma, Z. Feng, *Nat. Commun.* **2019**, *10*, 1711; d) D. Liu, X. Li, S. Chen, H. Yan, C. Wang, C. Wu, Y. A. Haleem, S. Duan, J. Lu, B. Ge, *Nat. Energy* **2019**, *4*, 512–518.
- [5] Y. Wang, D. Wang, Y. Li, *Adv. Mater.* **2021**, *33*, 2008151.
- [6] a) R. Jiang, L. Li, T. Sheng, G. Hu, Y. Chen, L. Wang, *J. Am. Chem. Soc.* **2018**, *140*, 11594–11598; b) K. Yuan, D. Lützenkirchen-Hecht, L. Li, L. Shuai, Y. Li, R. Cao, M. Qiu, X. Zhuang, M. K. Leung, Y. Chen, *J. Am. Chem. Soc.* **2020**, *142*, 2404–2412; c) L. Wang, C. Zhu, M. Xu, C. Zhao, J. Gu, L. Cao, X. Zhang, Z. Sun, S. Wei, W. Zhou, *J. Am. Chem. Soc.* **2021**, *143*, 18854–18858.
- [7] a) H. Shang, X. Zhou, J. Dong, A. Li, X. Zhao, Q. Liu, Y. Lin, J. Pei, Z. Li, Z. Jiang, *Nat. Commun.* **2020**, *11*, 3049; b) S. Ma, Z. Han, K. Leng, X. Liu, Y. Wang, Y. Qu, J. Bai, *Small* **2020**, *16*, 2001384; c) Y. Hou, M. Qiu, M. G. Kim, P. Liu, G. Nam, T. Zhang, X. Zhuang, B. Yang, J. Cho, M. Chen, *Nat. Commun.* **2019**, *10*, 1392.
- [8] a) A. Han, X. Wang, K. Tang, Z. Zhang, C. Ye, K. Kong, H. Hu, L. Zheng, P. Jiang, C. Zhao, *Angew. Chem. Int. Ed.* **2021**, *60*, 19262–19271; *Angew. Chem.* **2021**, *133*, 19411–19420; b) D. Yu, Y. Ma, F. Hu, C. C. Lin, L. Li, H. Y. Chen, X. Han, S. Peng, *Adv. Energy Mater.* **2021**, *11*, 2101242; c) M. Tong, F. Sun, Y. Xie, Y. Wang, Y. Yang, C. Tian, L. Wang, H. Fu, *Angew. Chem. Int. Ed.* **2021**, *60*, 14005–14012; *Angew. Chem.* **2021**, *133*, 14124–14131.
- [9] a) L. Jiao, G. Wan, R. Zhang, H. Zhou, S. H. Yu, H. L. Jiang, *Angew. Chem. Int. Ed.* **2018**, *57*, 8525–8529; *Angew. Chem.* **2018**, *130*, 8661–8665; b) L. Liu, Y. X. Yin, J. Y. Li, S. H. Wang, Y. G. Guo, L. J. Wan, *Adv. Mater.* **2018**, *30*, 1706216; c) J. Li, S. Chen, N. Yang, M. Deng, S. Ibraheem, J. Deng, J. Li, L. Li, Z. Wei, *Angew. Chem. Int. Ed.* **2019**, *58*, 7035–7039; *Angew.*

- Chem.* **2019**, *131*, 7109–7113; d) A. Zitolo, N. Ranjbar-Sahraie, T. Mineva, J. Li, Q. Jia, S. Stamatini, G. F. Harrington, S. M. Lyth, P. Krttil, S. Mukerjee, *Nat. Commun.* **2017**, *8*, 957.
- [10] C. Xia, Y. Qiu, Y. Xia, P. Zhu, G. King, X. Zhang, Z. Wu, J. Y. T. Kim, D. A. Cullen, D. Zheng, *Nat. Chem.* **2021**, *13*, 887–894.
- [11] J. Fan, M. Chen, Z. Zhao, Z. Zhang, S. Ye, S. Xu, H. Wang, H. Li, *Nat. Energy* **2021**, *6*, 475–486.
- [12] N. N. Greenwood, A. Earnshaw, *Chemistry of the Elements*, Elsevier, Amsterdam, **2012**.
- [13] a) S. S. Shinde, C. H. Lee, J.-Y. Jung, N. K. Wagh, S.-H. Kim, D.-H. Kim, C. Lin, S. U. Lee, J.-H. Lee, *Energy Environ. Sci.* **2019**, *12*, 727–738; b) S. H. Lee, J. Kim, D. Y. Chung, J. M. Yoo, H. S. Lee, M. J. Kim, B. S. Mun, S. G. Kwon, Y.-E. Sung, T. Hyeon, *J. Am. Chem. Soc.* **2019**, *141*, 2035–2045.
- [14] a) Y. Chen, R. Gao, S. Ji, H. Li, K. Tang, P. Jiang, H. Hu, Z. Zhang, H. Hao, Q. Qu, *Angew. Chem. Int. Ed.* **2021**, *60*, 3212–3221; *Angew. Chem.* **2021**, *133*, 3249–3258; b) F. Luo, A. Roy, L. Silvioli, D. A. Cullen, A. Zitolo, M. T. Sougrati, I. C. Oguz, T. Mineva, D. Teschner, S. Wagner, *Nat. Mater.* **2020**, *19*, 1215–1223.
- [15] a) C. Morant, J. Sanz, L. Galan, L. Soriano, F. Rueda, *Surf. Sci.* **1989**, *218*, 331–345; b) Y. Li, P. Wong, K. Mitchell, *Appl. Surf. Sci.* **1995**, *89*, 263–269.
- [16] Y. Chen, S. Ji, Y. Wang, J. Dong, W. Chen, Z. Li, R. Shen, L. Zheng, Z. Zhuang, D. Wang, *Angew. Chem. Int. Ed.* **2017**, *56*, 6937–6941; *Angew. Chem.* **2017**, *129*, 7041–7045.
- [17] a) M. Xiao, L. Gao, Y. Wang, X. Wang, J. Zhu, Z. Jin, C. Liu, H. Chen, G. Li, J. Ge, *J. Am. Chem. Soc.* **2019**, *141*, 19800–19806; b) B. Hammer, J. K. Nørskov, *Nature* **1995**, *376*, 238–240; c) J. K. Nørskov, F. Abild-Pedersen, F. Studt, T. Bligaard, *Proc. Natl. Acad. Sci. USA* **2011**, *108*, 937–943.

Manuscript received: July 4, 2022

Accepted manuscript online: July 13, 2022

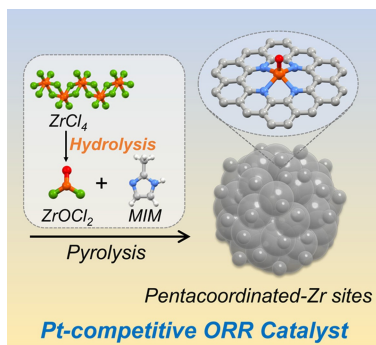
Version of record online: ■■, ■■

Research Articles

Oxygen Reduction Reaction

X. Wang, Y. An, L. Liu, L. Fang, Y. Liu,
J. Zhang, H. Qi, T. Heine, T. Li, A. Kuc,*
M. Yu,* X. Feng* **e202209746**

Atomically Dispersed Pentacoordinated-Zirconium Catalyst with Axial Oxygen Ligand for Oxygen Reduction Reaction



The first Zr-based single-atom catalyst with a stable pentacoordinated structure and high single-atom Zr loading is discovered. With the high-loading catalyst, the assembled zinc–air battery delivers a record-high power density among those of single-atom catalyst-based zinc–air batteries.